# Spray Coating Experiments: Setups and Methodologies

**The latest eBook from Advanced Optical Metrology. Download for free.**

*Spray Coating Experiments: Setups and Methodologies*, is the third in our Thin Films eBook series. This publication provides an introduction to spray coating, three article digests from Wiley Online Library and the latest news about Evident's Image of the Year Award 2022.

Wiley in collaboration with Evident, are committed to bridging the gap between fundamental research and industrial applications in the field of optical metrology. We strive to do this by collecting and organizing existing information, making it more accessible and useful for researchers and practitioners alike.

# Microfluidics-Based Force Spectroscopy Enables High-Throughput Force Experiments with Sub-Nanometer Resolution and Sub-Piconewton Sensitivity

*Yannic Kerkhoff, Latifeh Azizi, Vasyl V. Mykuliak, Vesa P. Hytönen, and Stephan Block\**

Several techniques have been established to quantify the mechanicals of single molecules. However, most of them show only limited capabilities of parallelizing the measurement by performing many individual measurements simultaneously. Herein, a microfluidics-based single-molecule force spectroscopy method, which achieves sub-nanometer spatial resolution and sub-piconewton sensitivity and is capable of simultaneously quantifying hundreds of single-molecule targets in parallel, is presented. It relies on a combination of total internal reflection microscopy and microfluidics, in which monodisperse fluorescent beads are immobilized on the bottom of a microfluidic channel by macromolecular linkers. Application of a flow generates a well-defined shear force acting on the beads, whereas the nanomechanical linker response is quantified based on the force-induced displacement of individual beads. To handle the high amount of data generated, a cluster analysis which is capable of a semi-automatic identification of measurement artifacts and molecular populations is implemented. The method is validated by probing the mechanical response polyethylene glycol linkers and binding strength of biotin–NeutrAvidin complexes. Two energy barriers (at 3 and 5.7 Å, respectively) in the biotin–NeutrAvidin interaction are resolved and the unfolding behavior of talin's rod domain R3 in the force range between 1 to ≈10 pN is probed.

## 1. Introduction

Over the past decades, several techniques have been established, which allow to apply forces on nanometer-sized biological objects, such as macromolecules, proteins or DNA, and to study biologically important processes, such as macromolecular interactions or force-induced changes in the conformation/structure of macromolecules, with single-molecule resolution.[1] The most prominent of these techniques are atomic force microscopy (AFM), optical tweezers (OT) and magnetic tweezers (MT), which use different approaches for force generation but have in common that they are capable of providing mechanical data originating from individual molecules.[2] In this way, they allow us to learn how mechanical forces modulate the structure and function of molecules, for example by opening cryptic binding sites within proteins.[3] Single-molecule methods also enable to probe for heterogeneities, such as rare events or transient states, in the mechanical response of an ensemble, which can be important features for biological systems, but are averaged out and therefore lost when applying ensemble-averaging approaches.

Hence, the introduction of single-molecule force techniques like AFM, OT, and MT enabled for completely new biophysical measurement schemes and allowed to study the force-related biological processes in unprecedented detail.[1] Nevertheless, as they probe the response of individual macromolecules, which is typically subject to notable, thermally driven fluctuations, it is necessary to probe this response multiple times in order to gain sufficient measurement statistics to make meaningful statements.[4] For AFM and OT, which are very limited in their capability to probe multiple individual interactions in parallel (low degree of parallelization), this is solved by repeating the measurement process, which may result in long measurement times. In contrast, the force generation in MT is compatible with a significant parallelization of the measurement process and implementations, in which hundreds of interactions have been simultaneously probed using MT have been described.[5] This concept has the advantage that significant amount of data is generated already in a single experimental run and also offers additional strategies to cope with heterogeneous samples, in which certain properties (such as the composition of interaction partners) show a notable distribution across the ensemble.

Such features are very interesting for investigations on complex biological systems, such as studies on how cells

Y. Kerkhoff, S. Block
Department of Chemistry and Biochemistry
Freie Universität Berlin
Arnimallee 22, 14195 Berlin, Germany
E-mail: stephan.block@fu-berlin.de
L. Azizi, V. V. Mykuliak, V. P. Hytönen
Faculty of Medicine and Health Technology
Tampere University
Arvo Ylpön katu 34, Tampere FI-33520, Finland
V. P. Hytönen
Fimlab Laboratories
Biokatu 4, Tampere FI-33520, Finland

The ORCID identification number(s) for the author(s) of this article can be found under https://doi.org/10.1002/smll.202206713.

ADVANCED
SCIENCE NEWS

www.advancedsciencenews.com

NANO · MICRO

small

www.small-journal.com

are able to transduce mechanical forces into biochemical signals.[6] It is known that mechanical forces have great effect on cellular behavior like adhesion, growth, maturation, and migration.[3,7–11] One of the many mechanosensors and mechanotransducers in cells is the force-bearing protein talin.[12–15] Talin is a force-sensitive protein consisting of 13 rod domains, which unfold at different forces (ranging between 5 and ≈40 pN) and therefore lead to complex unfolding patterns of the full-length proteins. Application of the before mentioned force spectroscopy methods (OT,[16] MT,[11,17,18] and AFM[3,19]) allowed to investigate this process in great detail, whereas an assessment of the unfolding of rod domain R3 remains challenging, which sets in at forces being comparable to the force resolution of OT and MT (≈1 pN) and out of the measurable range of AFM.

Inspired by these works, we aimed for designing a single-molecule force spectroscopy method, which combines the ability to apply very low to sub-piconewton forces (like in OT), while extending the high throughput capability of parallel MT, to meet the before mentioned criteria of sensitivity and statistical power. In principle, this is fulfilled by setups, in which microfluidics is used to generate hydrodynamic shear forces on interface-linked nanoparticles. One recent example was introduced by Block et al.,[20] in which fluorescent nanoparticles with defined sizes were linked to a fluid phase supported lipid bilayer (SLB) in a microfluidic channel. Application of total internal reflection fluorescence (TIRF) microscopy allowed us to track the force-induced motion of supported lipid bilayer (SLB)-linked nanoparticles with single-nanoparticle resolution. Analyzing this motion provided a new means to determine the shear force acting on a nanoparticle directly from its trajectory and hence to determine the impact of nanoparticle size and channel flow rate on the generated shear force. In this way, the authors demonstrated that this setup enables to generate very small forces (ranging between femtonewtons to piconewtons) and allows us to sensitively probe the action of such small forces on hundreds of individual nanoparticles in parallel, providing a high parallelization of the force sensing process.

In this work, we aim to translate this setup to nanoparticles that have been stably linked to the bottom of the microfluidic channel, as this should allow for highly parallelized force measurements (addressing up to thousands of interactions in parallel) with an outstanding sub-piconewton force sensitivity. As in our previous study, we use a combination of total internal reflection fluorescence (TIRF)-based optical video microscopy and a PDMS-based microfluidic channel (width: 150 μm; height: 100 μm), which was bonded to a thin glass slide (forming the bottom of the microfluidic channel; **Figure 1**a). To test our hypothesis, we attached fluorescent beads of known size to the glass surface by a linker and studied bead displacement and bead detachment as a function of the applied shear forces (Figure 1b). This data provided information on the nanomechanical properties of the linker (bead displacement) or the binding strength between bead and interface (bead detachment), which will be discussed in detail in the following paragraphs. We applied these two measurement modalities to two well-established model systems (nanomechanics of polyethylene glycol, PEG, and binding strength of the ligand–receptor

interactions biotin–NeutrAvidin), which formed the basis for an assessment on the performance of this flow-based force spectroscopy approach. Finally, we applied this new tool to investigate the unfolding of talin's rod domain R3, further demonstrating the benefits offered by combining high force resolution (<pN) with high parallelization of the measurement process.
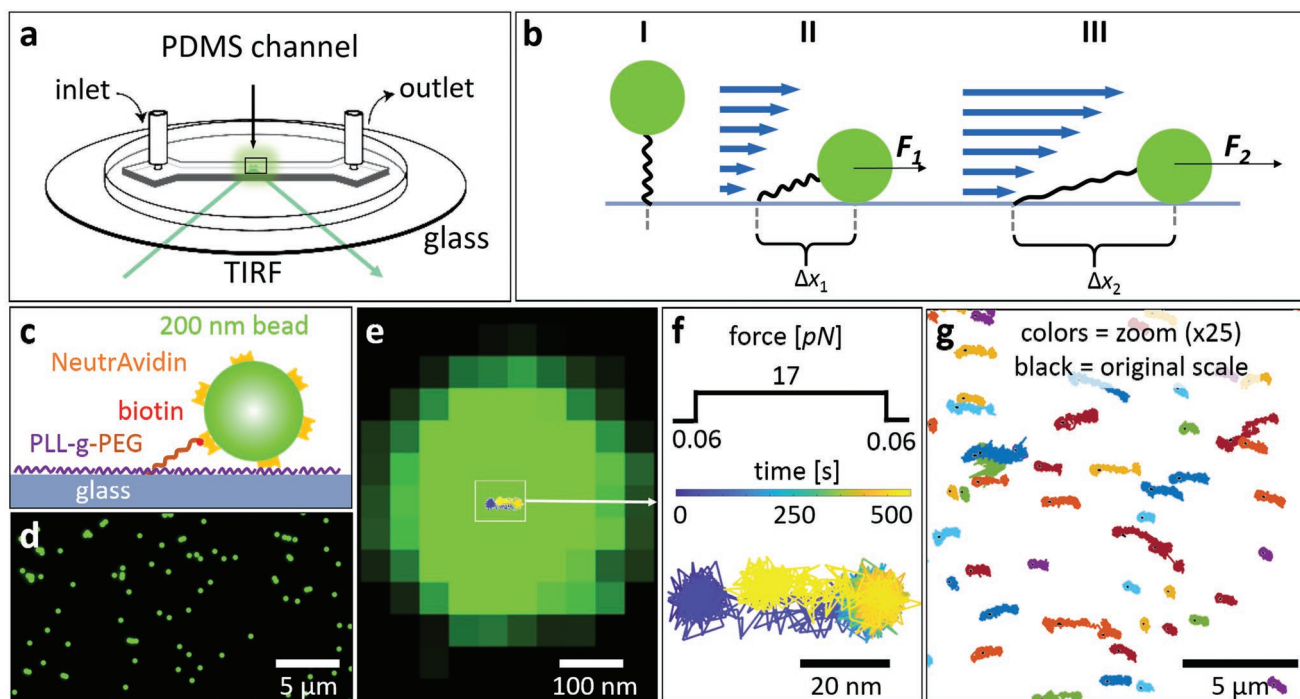
## 2. Results and Discussion

### 2.1. Stretching of PEG-Polymer

In a first set of experiments, we studied the nanomechanics of PEG-based linkers (Figure 1c), which allowed us to evaluate our approach using a well-studied system. To this end, we functionalized the bottom of the microfluidic channel using block-copolymers consisting of a 20 kDa poly-L-lysine chain (PLL) coupled to a 3.4 kDa PEG chain, which bind via electrostatic interactions of the positively charged PLL to the negatively charged glass surface. As a very small fraction of the PEG chains were equipped with a biotin moiety (see Experimental Section for details), it was possible to stably link monodisperse, NeutrAvidin-coated fluorescent polystyrene beads (diameter: 200 nm) to the interface using the highly specific biotin–NeutrAvidin interaction. In this way, thousands of fluorescent beads were immobilized in the field of view (FoV) of our microscope ($135 \times 135$ μm$^2$) and subjected to flow-induced shear forces, which allowed for a high parallelization of the measurement process.

This is demonstrated in Figure 1d, which represents ≈7% of the microscope's FOV and shows 80 beads out of a sample carrying approximately 1100 beads per FoV. The high brightness of the beads enables us to achieve single shot localization accuracies below 1 nm (see Section S1, Supporting Information) and hence to detect sub-nanometer bead displacements as a function of the applied flow rate (Figure 1e), provided that drifts of the sample surface (e.g., caused by changes in the flow conditions) are correctly compensated (see Section S1, Supporting Information, for more details on this procedure).

The application of a block-shaped force profile leads, as expected, to a block-shaped displacement response of the beads (Figure 1f). In this example, the measurement started with the application of a very low shear force (0.06 pN) to the bead, which is so small that the bead's center position (*x*- and *y*-coordinates in the image) fluctuates around the attachment point of the linker. After 50 s, the force was increased to 17 pN, leading to a 40 nm displacement of the bead's center position in flow direction (cyan to orange). After application of this force for 400 s, the shear force was reduced again to 0.06 pN for 50 s, allowing the bead to return near its initial position (yellow, deviation ≈13 nm). This almost fully reversible response indicates that the bead is elastically linked to glass surface, which is a finding that is representative for nearly all of the 1100 analyzed beads (a fraction of 50 tracks from a randomly chosen part of the FoV is shown in Figure 1g).

Obviously, all beads given in Figure 1g showed a force-induced displacement in flow direction, whereas the extent of the displacement varies between the beads. This means that some of the beads showed a larger displacement, while
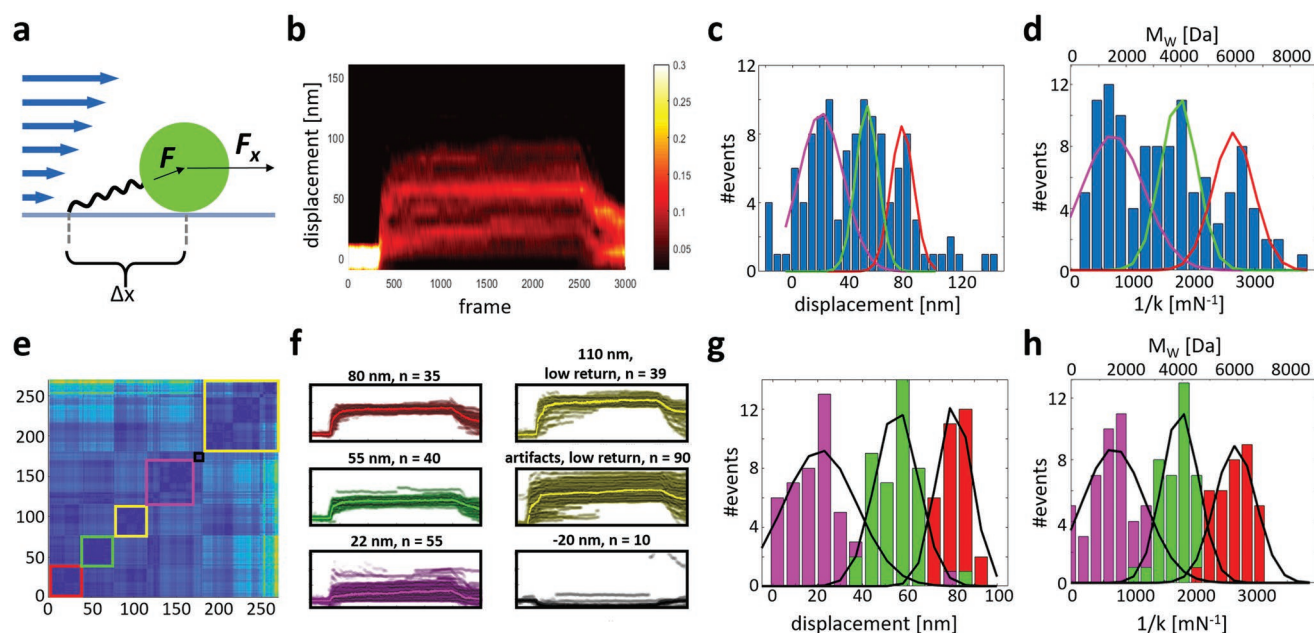
**ADVANCED
SCIENCE NEWS**

www.advancedsciencenews.com

NANO · MICRO

**small**

www.small-journal.com

**Figure 1.** Scheme of the microfluidics-based force spectroscopy method. A 150 µm wide microfluidic channel with in- and outlet is embedded in a PDMS stamp, bonded on a glass slide, and mounted on a TIRF microscope (a). In general, fluorescent beads (green) are attached to a linker (black), which is bound to the glass (b; not drawn to scale), and hover over the surface if no flow is applied (b-I). Low flow rates generate relatively low forces ($F_1$), and the bead is pushed in flow direction ($\Delta x_1$) and moved toward the surface (b-II). High flow rates apply relatively high forces ($F_2$) and push the bead further ($\Delta x_2$), resulting in a stretching of the linker (b-III), which can be quantified based on the bead displacement. As the flow is laminar and as the distance between the beads is typically much larger than their diameter, any modification to the flow (caused by the hydrodynamic interaction with the beads) will be quickly screened out and all beads will experience the same shear rate. To probe the nanomechanics of PEG (c), the glass surface is coated with block copolymers of poly-L-lysine (purple) and PEG (brown), a small fraction of which presents biotin moieties (red) at the PEG chain and can be used to link NeutrAvidin-coated 200 nm fluorescent bead (green). A zoom in the field of view (FoV) of the TIRF microscope of a sample having about 1100 linked beads in total per FoV (d). An overlay of the intensity distribution of one representative bead with its displacement trajectory (generated by application of a block-shaped force profile: 0.06 → 17 → 0.06 pN, see also (f)) indicates that the high localization accuracy of our approach allows us to follow even very small bead displacements (e). In this representative displacement trajectory (f), the blue color shows the initial position of the bead center at the low force of 0.06 pN, followed by a displacement of the bead of about 40 nm upon application of 17 pN shear force (color shift from cyan to green and orange). Afterward, the bead returns near its initial position due to the reduction of the shear force to 0.06 pN (yellow). As thousands of beads can be tracked per FoV, such measurements lead to thousands of force-induced displacement trajectories, a small fraction of which is shown in (g). For visualization reasons, these trajectories were sized up by the factor of 25, whereas their central position was preserved ((g), black dots).

others seemed to be nearly immobile. To quantify this effect, we calculated a density map of observed bead displacements from block-wise stretched linkers (Figure 1c–g). As a notable number of displacements curves terminated before the end of the experimental run (indicative for force-induced detachment of the corresponding bead), we restricted this analysis to all displacements curves, which covered the entire experimental run and which followed the block-wise force response (i.e., showed return to the initial position). Calculating the density map of these displacement curves (**Figure 2**b) shows that the displacement values are not evenly distributed, but exhibited only specific values (≈22, 55, and 80 nm). These distinct populations are also clearly visible in the histogram of bead displacement values (Figure 2c) and indicate that the different bead displacement populations are caused by differences in the nanomechanical response of the linkage (i.e., by differences in the number of linkers engaged by the beads, as will be shown below).

In order to accurately quantify the nanomechanical response from the observed displacement of the bead's center position, we model the system as schematically depicted in Figure 2a and analyzed in detail in Section S2, Supporting Information. In a typical measurement, the linkers have an equilibrium end-to-end extension that is much smaller than the radius of the monodisperse beads. This feature generates a geometrical constraint that allows linkers to connect to the bead only within a relatively small area of the bead's apex. Hence, even if beads are linked by multiple linkers to the interface, they will be at close proximity to each other (with respect to the length scale of the bead) and hence experience essentially the same mechanical load.

As an additional consequence, the surface separation between the bead and the interface will be small in comparison to the bead radius and, as the beads show a monodisperse size distribution, the flow will generate a shear force, $F_x$, which is the same for all beads. Nevertheless, the actual force acting in

**ADVANCED
SCIENCE NEWS**

www.advancedsciencenews.com

NANO · MICRO

**small**

www.small-journal.com

**Figure 2.** Stretching of PEG-linkers revealed linker valency indicated by distinct populations in displacement, molecular weight, and spring constant. The bulk flow applies a shear force on the bead in flow direction, $F_x$, which loads the linker with the loading force $F$ and results in a bead displacement $\Delta x$ (a). A density map of 113 bead displacement curves (b) shows accumulations of curves (red) in distinct regions (approximately at displacements of 22, 55, and 80 nm, respectively). The histogram of these displacements at saturation (c) as well as of the corresponding values for linker spring constant and apparent linker molecular weight ((d), see main text for details) shows three distinct populations. The solid lines in (c) and (d) give Gaussian fits that originate from the data analysis summarized in (e–h). In this data analysis, the beads have been automatically assigned to distinct populations based on a cluster analysis applied to the observed bead displacement curves. This procedure (described in detail in Section S3, Supporting Information) yields a symmetric 2D similarity map (e), which provides the similarity of two displacement curves (given by their ID values on the x- and y-axis, respectively) based on the calculation of the standard deviation of their displacement difference. This similarity measure is color coded in (e), in which high to low similarity is indicated by colors ranging from blue to yellow. Applied to all 260 displacement curves from a representative experiment, the cluster analysis identified six distinct cluster groups (red, green, yellow, purple, black squares in (e)), whereas the assigned displacement curves indeed behave very similar within the corresponding cluster as shown in (f), which provides an overlay of all assigned displacement curves and their ensemble average as thick solid curve. Enlarged versions of (e) and (f) are given in the Supporting Information. This analysis provides three populations showing the displacement behavior already observed in (b) and (c), but also three additional populations, the curves of which either contain obvious measurement artefacts (such as lack of return to the initial position at very low flow rates, yellow population) or indicate immobile beads (showing no notable displacement upon application of a force, black population). Histogram of the median displacement value ((g), taken at the saturation regime of the displacement curves from the red, green, and purple populations) as well as the corresponding values of linker spring constant and apparent linker molecular weight (h) are well described by Gaussian fits and yield distributions consistent with (c) and (d). Hence, the cluster analysis enables to decompose the full data set into individual bead populations based on their nanomechanical behavior and to efficiently identify artefact-bearing displacement curves within the data.

direction of the linker(s), $F$, depends on the angle between the linker(s) and the horizontal (i.e., the surface; see Figure 2a). This means that only a fraction of the full shear force $F_x$ (that acts on the bead) will be applied to the linker(s) and that this fraction increases with increasing bead displacement ($\Delta x$), as this process will reduce the angle between the linker(s) and the surface. As shown in Section S2, Supporting Information, the force acting in direction of the linker(s), $F$, as well as the extension of the linker(s) due to this force can be calculated from the bead displacement, $\Delta x$, under the assumption that the bead always touches the surface.

This assumption is plausible, as a shear force acting on "hovering" beads (not touching the surface) will generate a torque that pushes the beads toward the interface until contact has been achieved. We will revisit this assumption at the end of this section. Applying the model discussed in Section S2, Supporting Information, allows us to calculate for each bead the force acting in direction of the linker(s), $F$, and the

force-induced extension of the linker(s), $L$, from the measured bead displacement $\Delta x$ (see Figure S1, Supporting Information, for one representative example of this procedure). Application of this model to the three populations of Figure 2c, which exhibit peaks at displacement values of $\Delta x \approx 22$, 55 and 80 nm, leads to linker extensions $L \approx 2.4$, 14.1 and 28.0 nm and (total) loading forces $F \approx 3.6$, 8.2 and 10.6 pN, respectively. This example demonstrates the fact that the displacement $\Delta x$ is always larger than the actual linker extension $L$, which is a consequence of force-induced motion of the bead around the anchoring point of the linker(s) and amplifies small values of the linker extension to much larger values of $\Delta x$.

In order to test the hypothesis that the observed populations are generated by differences in the nanomechanical behavior of the linker(s), we used the observed values of linker extension $L$ caused by the loading force $F$ to calculate the stiffness of the linker(s) in terms of the spring constant, $k = F/L$. Assuming that the PEG linkers are well described by the freely jointed

**ADVANCED
SCIENCE NEWS**

www.advancedsciencenews.com

**NANO · MICRO
small**

www.small-journal.com

chain model,[21] an assumption that has been validated for PEG chains in aqueous solutions in a variety of studies,[22,23] it is possible to relate the observed spring constant $k$ to the molecular weight of the linker, $M_w$, via the relationship:[21]

$$M_\mathrm{w} = \frac{3 \cdot k_\mathrm{B} \cdot T}{\kappa_\mathrm{K} \cdot k} \cdot \frac{M_\mathrm{EG}}{L_\mathrm{EG}} \tag{1}$$

in which $k_\mathrm{B}$ denotes Boltzmann's constant, $T$ the temperature (in Kelvin), and $\kappa_K$ the Kuhn length of PEG ( = 0.7 nm)[22,23] while $M_\mathrm{EG}$ and $L_\mathrm{EG}$ denote the molecular weight and physical length of a PEG monomer (44 Da and 0.3 nm, respectively). A histogram of observed (theoretical) molecular weights of the linker (Figure 2d) also exhibits distinct populations with average weights of 1.5, 3.5, and 6.1 kDa. The calculated molecular weight of the softest (red) population (≈6.1 kDa) is higher than the molecular weight of the PEG target (3.4 kDa) and indicates that application of a shear force does not only stretch the 3.4 kDa PEG chain but also part of 20 kDa PLL chain. The green and the purple population show apparent molecular weights of ≈3.5 and ≈1.5 kDa, respectively. This observation suggests that these populations correspond to beads linked by 2 and 3 PEG-based linkers, as this increases the (overall) linker spring constant by a factor of 2 and 3, respectively, and lead to apparent molecular weights being only one half and one third of the true molecular weight of a single linker (see Equation (1)). We therefore conclude that the distinct molecular populations observed in the histograms of bead displacement and spring constant/ apparent molecular weights can be explained by differences in the number of linkers engaged by the respective beads.

Although this analysis workflow allowed to address the nanomechanics of the PEG-based linkers, the analysis of the obtained data turned out to be challenging (despite the simplicity of this system), as the difference in the binding stoichiometry of the beads caused broad distributions and complex morphology of the derived displacement curves. Furthermore, visual inspection of the displacement curves showed that a notable fraction of these curves contained obvious measurement artefacts and had to be (manually) removed from the data analysis. Owing to the high data throughput of the method, which allows us to quickly perform many experimental runs providing hundreds to thousands of displacement curves per run, this manual inspection turned out to be the bottleneck of the analysis. To address this limitation, we developed an automated cluster analysis, which enabled to automatically define and classify the distinct molecular populations as well as artifacts-bearing or non-responsive curves (Figure 2e, for details see Section S3, Supporting Information). In short, this analysis picks all possible pairs of two displacement curves from the data and calculates for each pair the standard deviation $sd$ of the difference of their displacement curves. This information is stored in a 2D matrix (in which the $x$- and $y$-dimension correspond to the IDs of the two displacement curves of a particular pair) and afterward, displacement curves with high similarity (indicated by low $sd$ values) are grouped together.

The grouping result can be visualized in a 2D color map (Figure 2e), indicating similar displacement curves in blue and distinct ones in yellow. This cluster map visualizes the distinct populations (indicated by red, green, yellow, purple, and black squares in Figure 2e) and therefore provides an assignment

of displacement curves into populations of similar behavior that can be quickly validated by manual inspection. This tool turned out to be very valuable, as it allowed an almost automatic identification of artefact-bearing displacement curves and as it correctly decomposed the complex displacement distributions of Figure 2c into individual populations differing in the nanomechanical behavior (red, green, and purple populations in Figure 2f,g). This showed that the cluster analysis allows for an automated reliable classification of molecular populations in such complex data sets, which was further validated by correct reconstruction of simulated FEC populations (for details see Section S3.2, Supporting Information).

## 2.2. Binding Strength of Biotin-NeutrAvidin Interaction

Beside the displacement curves covered above, which showed a constant displacement during force application and return afterward, we also observed displacement curves that terminated before the end of an experimental run (caused by bead detachment) and/or showed sudden increases in the displacement value without any change in the applied shear force (**Figure 3**a,b). These features can be explained by a decrease in the number of linkers engaged by the corresponding bead, as some of the biotin–NeutrAvidin interactions, which are used to connect the beads to the linkers, can rupture due to the applied force.[24–26] If the bead is linked to $n_\mathrm{l}$ linkers, the loading force ($F$ in Figure 2a) is distributed over several linkers. As each linker will be loaded (on average) by $F/n_\mathrm{l}$, the bead displacement will increase with decreasing number of engaged linkers ($n_\mathrm{l}$). Hence, if one linker detaches, the bead will not completely rip from the surface but will show a step toward larger values in the displacement curve, as long as the bead is linked via at least one linker. If the last linker detaches, the bead will detach from the surface, causing the displacement curve to terminate before the end of the experimental run. This results in displacement curves, which show transitions between distinct displacement plateaus (Figure 3a). In order to assign the observed displacement plateaus to the number of acting linkers ($n_\mathrm{l}$), we note that our nanomechanical analysis of the PEG-based linkers (given in the previous section) provides us with the distributions of displacement values of beads being linked by one to three PEG-based linkers (shown in Figure 2g). This information enables us to define intervals of displacement values that correspond to beads being linked by $n_\mathrm{l}$ linkers (red lines in Figure 3a,b) and hence to translate the time-dependent displacement curves into time-dependent changes of the $n_\mathrm{l}$ value. Similar to other force spectroscopic approaches, this approach ensures that only displacement curves are included in the follow-up analysis, which exhibit a nanomechanical behavior matching with the employed PEG-based linkers.

The duration of plateaus of constant $n_\mathrm{l}$ value gives the residence time of the corresponding linking state and thus contains information on the force-dependent stability of the biotin–NeutrAvidin interaction. In a first step, we apply this analysis to all displacement curves showing rupture events of single biotin–NeutrAvidin interactions, that is, corresponding to the 3 transitions of $n_\mathrm{l} = 3$ to 2, 2 to 1, and 1 to 0 (bead detachment). For a random detachment processes (i.e., for transition
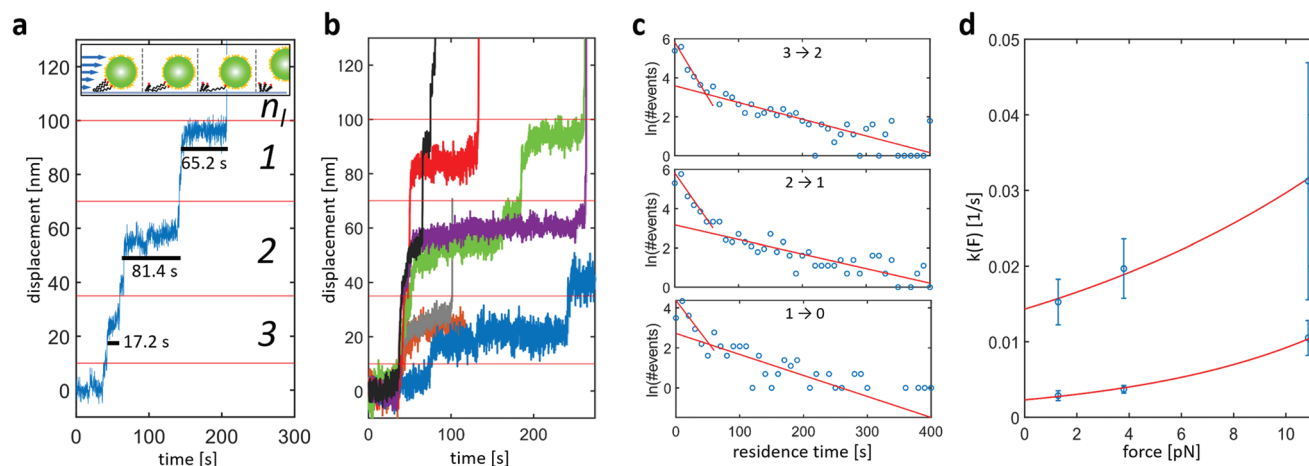
**Figure 3.** Detachment kinetics of multivalent biotin–NeutrAvidin complexes. A representative bead displacement curve showing three distinct displacement plateaus (a), which were caused by a sequential detachment of three PEG-linkers. This detachment requires rupture of individual biotin–NeutrAvidin interactions, as schematically indicated in the inset. Measuring the duration of individual rupture processes (black bars in (a)) allows us to determine the residence time associated for transitions from $n_l = 3$ to 2 ($3 \rightarrow 2$), from 2 to 1 ($2 \rightarrow 1$) as well as for release of the final interaction ($1 \rightarrow 0$). The sequential detachment of linkers was observed in many displacement curves, as indicated by the example of 7 representative curves shown in (b). Extracting the residence times (as shown in (a)) from all such curves allowed to determine the residence time distributions for the different transitions ($3 \rightarrow 2$, $2 \rightarrow 1$, and $1 \rightarrow 0$), which typically showed two distinct exponential decays and therefore indicates that each of these processes decays with 2 transition rates (c). These transition rates ($k_s$ and $k_f$) increase with increasing loading force per linker (d), which can be well-described by the Bell model (solid line). Application of this model revealed two energy barriers for the energy landscape of the biotin–NeutrAvidin interaction, having potential widths of 5.7 and 3.0 Å and zero-force off-rates of $2.3 \times 10^{-3}$ and $14.3 \times 10^{-3}$ s$^{-1}$, respectively.

that are statistically uncorrelated), the residence time distributions are expected to show an exponential decay, the decay rate of which corresponds to the transition rate. Plotting the three residence time distributions on a semi logarithmic scale (Figure 3c) indeed reveals exponential decays (indicated by straight lines in this representation), but in fact two distinct decay rates for each of the three transitions. Hence, the biotin–NeutrAvidin interaction decays in our experiments with two transition rates, which can be determined by linear fits of the residence time distributions (red lines in Figure 3c).

In order to determine the impact of the loading force on the failure rate of a single biotin–NeutrAvidin interaction, one has to account for the difference in the number of acting interactions of the three transition processes. If the transition starts with $n_l$ linkers, one has to take into account that only the fraction $F/n_l$ of the total loading force acts on a single linker (i.e., on a single biotin–NeutrAvidin interaction). Furthermore, since $n_l$ interactions are present, the observed transition rate is $n_l$ times larger than the rate of rupture (off-rate) of a single biotin–NeutrAvidin interaction. Accounting for these effects enabled to determine the impact of loading force on the off-rate of a single biotin–NeutrAvidin interaction (Figure 3d). As two transition rates were observed in the residence time distributions, this plot contained two force-dependent off-rates, each of which is well described by Bell's theory.[27] This analysis suggests an energy landscape that consists of at least two energy barriers, having potential widths of 5.7 and 3.0 Å and zero-force (equilibrium) off-rates of $2.3 \times 10^{-3}$ and $14.3 \times 10^{-3}$ s$^{-1}$, respectively. The widths of these energy barriers are consistent with AFM-based force spectroscopy experiments,[26,28,29] whereas the zero-force off-rates are in the lower range of reported values.[26,28–31]

In addition to these events, in which a single biotin–NeutrAvidin interaction dissociates, the recorded displacement

curves also contain events that correspond to the simultaneous failure of multiple biotin–NeutrAvidin interactions. Most often, we observed the transitions $n_l = 3$ to 1 and $n_l = 2$ to 0, in which wo biotin–NeutrAvidin interactions dissociated simultaneously. The corresponding residence time distributions are given in Figure S7, Supporting Information, and also show two distinct exponential decays, which are indicative for the presence of two decay rates. These decays should be describable based on the known dynamics of the (single step) transitions $n_l = 3$ to 2, 2 to 1, and 1 to 0. For example, if $k_{3 \rightarrow 2}$ and $k_{2 \rightarrow 1}$ denote the transition rates for the transitions $n_l = 3$ to 2 and 2 to 1, the transition rate $k_{3 \rightarrow 1}$ (corresponding to $n_l = 3$ to 1) should fulfil the rate equation: $1/k_{3 \rightarrow 1} = 1/k_{3 \rightarrow 2} + 1/k_{2 \rightarrow 1}$. The situation is, however, more complex, as a single biotin–NeutrAvidin interaction exhibited in our experiments always two single step transition rates ($k_f$ and $k_s$ in Figure 3d, which are associated to the barriers at 3.0 and 5.7 Å, respectively), so that the occurrence of four transitions rates is to be expected for the simultaneous failure of two biotin–NeutrAvidin interactions: $1/k_{3 \rightarrow 1,ff} = 1/k_{3 \rightarrow 2,f} + 1/k_{2 \rightarrow 1,f}$, $1/k_{3 \rightarrow 1,fs} = 1/k_{3 \rightarrow 2,f} + 1/k_{2 \rightarrow 1s}$, $1/k_{3 \rightarrow 1,sf} = 1/k_{3 \rightarrow 2,s} + 1/k_{2 \rightarrow 1,f}$ and $1/k_{3 \rightarrow 1,ss} = 1/k_{3 \rightarrow 2,s} + 1/k_{2 \rightarrow 1,s}$. As $k_f$ and $k_s$ differ by almost one order of magnitude for all transitions (Figure 3d), the rates $k_{3 \rightarrow 1,fs}$, $k_{3 \rightarrow 1,sf}$, and $k_{3 \rightarrow 1,ss}$, will be dominated by the slower rate constant ($k_{2 \rightarrow 1s}$ and $k_{3 \rightarrow 2s}$, respectively) and will exhibit similar values, which cannot be resolved individually in a residence time distribution. It is therefore expected that the residence time distributions extracted from the simultaneous failure of two biotin–NeutrAvidin interactions show two exponential decays with decay rates given by $k_{3 \rightarrow 1,ff}$ and $k_{3 \rightarrow 1,fs} \approx k_{3 \rightarrow 1,sf} \approx k_{3 \rightarrow 1,ss}$. This reasoning matches well with the experimental observation (see Figure S7, Supporting Information) and highlights the complexity in unbinding dynamics addressable by our method.

**ADVANCED
SCIENCE NEWS**
www.advancedsciencenews.com

NANO · MICRO
**small**
www.small-journal.com

### 2.3. Nanomechanics of Talin's Rod Domain R3

After evaluating the performance of our microfluidics-based force spectroscopy approach, we set out to apply it to study the nanomechanics of proteins, which start to unfold already if subjected to piconewton forces. In particular, we aimed for probing the unfolding behavior of talin's rod domain R3, the characterization of which proved to be very challenging even for highly sensitive force sensing techniques such as OT and MT. To this end, we integrated into our assay a recently described fragment containing talin's rod domains R1 to R3,[19] which has been intensively characterized using MT and AFM in the past and showed unfolding of R3 for forces being on the order of 5 pN.[19,17] In our measurements, we employed the protein construct introduced by Haining et al. (termed R1-3 in the following),[19] in which the rod domains R1 to R3 are integrated between two repeats of titin's I27 domain (which generated a nanomechanical signature in their AFM measurements), whereas the N- and C-termini of the whole construct were functionalized with a HaloTag and cysteine residue, respectively. Hence, the R1-3 construct can be understood as the following polyprotein: HaloTag-(I27)$_2$-R1-R2-R3-(I27)$_2$-His$_6$-Cys. Furthermore, a variant of this construct was available for our measurements (termed I27 in the following), which consists only of the I27 domain repeats: HaloTag-(I27)$_8$-His$_6$-Cys. As unfolding of I27 requires forces exceeding 50 pN,[32] the protein construct I27 cannot be unfolded with the forces achievable in our setup (≈20 pN) and therefore serves as negative control in our unfolding measurements. Furthermore, R1 and R2 unfolding has been reported to occur for loading forces well beyond 10 pN,[17] making unfolding of these two rod domains in our experiments a possible yet unlikely process.

Both protein constructs were integrated into our assay by coupling the constructs to monodisperse, fluorescent beads (diameter: 200 nm) via the HaloTag moiety, whereas the cysteine residue was used to biotinylate the constructs and to link the biotinylated protein constructs to NeutrAvidin moieties attached to the bottom of a microfluidic channel (as described in the Experimental section). The displacement of these beads was recorded using a flow profile that generated the following sequence of loading forces $F$: 0.3, 0.7, 1.3, 2.8, 6.0, and 0.3 pN (**Figure 4**a). As in our stretching experiments involving PEG chains, we again observed a broad distribution of bead displacement responses, which required the application of the above-mentioned cluster analysis to identify populations of similar nanomechanical behavior as well as artifact-containing displacement curves. We typically observed 4 populations, which reproduced well between independent measurement runs and which were attributed to beads being linked to the surface by one, two, three, or more protein constructs (Figure 4a showing the ensemble-averaged displacement curves of the individual populations). This interpretation is supported by the observed spring constants being consistent with a recent investigation.[17] To simplify the analysis, we will restrict the following assessment to the population corresponding to a single construct linking the bead to the surface. Comparing the individual displacement curves of this population with the ensemble-averaged response yields several candidate curves, which exhibit significantly larger displacements (i.e., potential unfolding events) in comparison to the ensemble answer. We therefore continued to extract for each displacement curve the linker extensions (using the model described in Section S2, Supporting Information) as a function of the applied shear force and compared these distributions for the R1-3 and the I27 constructs (Figure 4b and Figure S6, Supporting Information).
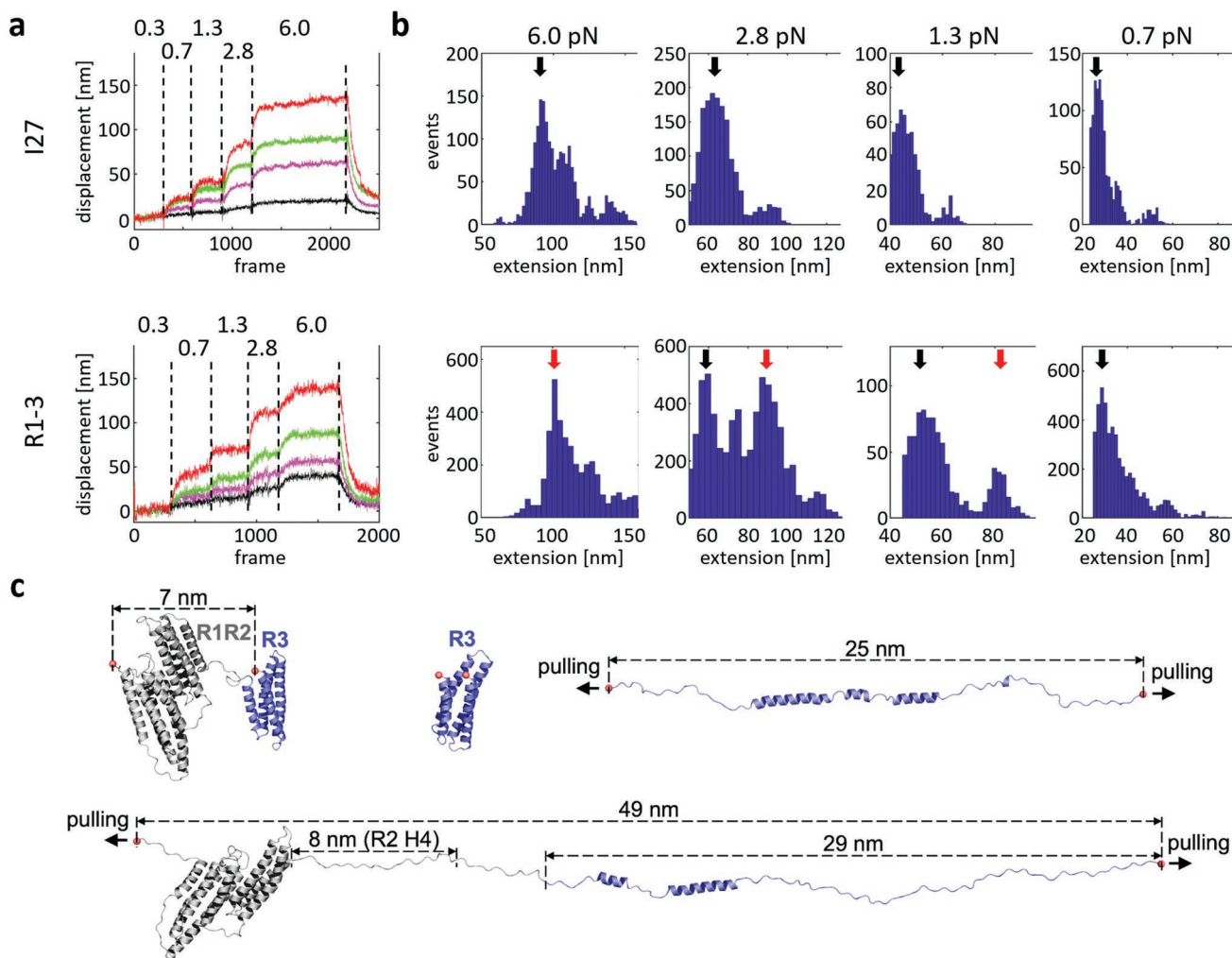
The extension distributions obtained from the I27 construct are mainly given by a single peak, which indicates the extension value of a fully folded construct (black arrows in Figure 4b). In addition, the I27 distributions also show few minor peaks, which contribute less than 10% of the observed events and are attributed to minor errors in the determination of the displacement. The extension distributions obtained from the R1-3 construct show, however, a much more complex structure. While for loading forces of 0.7 and 6 pN only one peak is observed, at least one additional population is observed for loading forces of 1.3 and 2.8 pN (red arrows in Figure 4b), which is missing for the I27 construct. The change in extension between the two populations is 27.8 and 31.8 nm (at 1.3 and 2.8 pN, respectively), which matches very well with the expected increase in construct extension upon unfolding of the rod domain R3 (as determined in steered molecular dynamics simulations; Figure 4c) and is close to experimentally observed values (≈25 nm).[17] Hence, this population is attributed to fully unfolded R3.

This analysis reveals that 21% and 64% of the R1-3 constructs started to unfold at 1.3 and 2.8 pN, respectively, indicating that notable R3 unfolding can already be observed for loading forces at the 1 pN scale. At 6 pN, we observe, as for the I27 construct, only a single population, which we attribute to fully unfolded R1-3 construct. This interpretation is supported by the trend in the unfolding at 1.3 and 2.8 pN as well as by a notable shift in the peak position between the I27 and the R1-3 construct (≈20 nm).

## 3. Conclusion

In our study, we introduced a microfluidics-based force spectroscopy technique, which allowed us to quantify the nanomechanical behavior of polymers and protein constructs as well as the binding strength of a ligand–receptor interaction. The performance of this technique was evaluated by quantifying the molecular spring constant of PEG-containing linkers, which allowed us to validate the measurement and data analysis procedure using a well-studied system. This assessment indicated that the technique combines high parallelization of the measurement process (following the response of up to thousand beads in parallel) with outstanding spatial resolution (sub-nanometer localization accuracy) and sub-piconewton force sensitivity (see Table S1, Supporting Information, for further details). Nevertheless, it also revealed that the close vicinity of the beads to the surface of the microfluidic channel causes a notable fraction of displacement curves to contain artifacts, which have to be identified and excluded from further data analysis. To address this problem, we integrated a cluster analysis, which assigned the recorded displacement curves into populations according to similarities in their displacement behavior. This procedure did not only enable to semi automatically identify artifact-containing displacement curves but

**ADVANCED
SCIENCE NEWS**

www.advancedsciencenews.com

NANO · MICRO

**small**

www.small-journal.com

**Figure 4.** Unfolding of talin's rod domain R3. Linking the beads using protein constructs containing (talin rod domains R1 to R3; R1-3) or lacking (I27) talin's rod domain insert yielded shear force-induced displacement curves that showed a broad distribution of displacement values. As in the case of PEG-linker stretching (Figure 2), application of the cluster analysis yielded distinct populations ((a), showing the ensemble-averaged displacement curve), which correspond to beads that are linked by one (red), two (green), three (purple) or more (black) constructs to the surface. Analyzing all displacement curves of beads being linked by a single construct (red in (a)), yielded information on the extension of the constructs (b) as a function of applied loading force (as indicated in (b)). While the extension distributions of I27 typically showed only one major peak (black arrow), which is consistent with a construct that cannot be unfolded below loading forces of 50 pN, an additional peak is observed for the R3-containing construct (R1-3, red arrows), which is attributed to unfolded R3 (as discussed in the main text). c) Talin rod R1-3 and R3 unfolding in steered molecular dynamics. R1-3 construct revealed complete unfolding of R3 before unfolding of R1-2 domains, however, due to high force applied in the constant velocity pulling at 2 nm ns$^{-1}$, the C-terminal helix (H4) of R2 unfolded before the complete unfolding of R3. The total end-to-end distance of R1-3 construct with unfolded R3 is 49 nm, while contribution of completely unfolded R3 (residues 796–909) is 29 nm, and contribution of unfolded R2 H4 alone is 8 nm. The end-to-end distance of folded R1-3 is 7 nm. Using slower pulling speed at 0.1 nm ns$^{-1}$ for unfolding of R3 domain alone, the R3 domain preserved more helicity after complete unfolding of tertiary structure, with the end-to-end distance of 25 nm. Terminal C-alpha atoms used for pulling are shown as spheres.

also to identify populations that differ in their nanomechanical response (due to difference in the number of engaged linkers), which was key to analyze the complex data sets obtained by this technique. As an application of this new technique, we probed the dynamics of force-induced bond failure of the ligand–receptor interaction biotin–NeutrAvidin, which was dominated by two energy barriers in our constant force spectroscopy setup. Furthermore, we used this technique to study the unfolding behavior of a talin's rod domain R3, which indicated notable unfolding to occur at smaller forces (1 pN scale) than previously believed. These experiments clearly demonstrate the potential

of this microfluidics-based force spectroscopy technique, especially for the characterization of even more complex systems than covered in this study.

Evaluation of this technique showed, however, that the non-covalent immobilization strategy based on the biotin-NeutrA-vidin interaction is, contrary to our initial expectations, not strong enough even for force in the 5 pN range. Although this allowed us to study the bond failure of ligand–receptor inter-actions, this immobilization strategy causes a notable fraction of tracked beads to detach before the end of an experimental run, thereby significantly lowering the data throughput and

ADVANCED
SCIENCE NEWS
www.advancedsciencenews.com

NANO · MICRO
small
www.small-journal.com

making the data analysis more complex. In future experiments, we will therefore switch to covalent immobilization strategies in order to avoid this problem.

## 4. Experimental Section

*Chemicals*: Polydimethylsiloxane (PDMS), Biotin-maleimide, Tris(2-carboxyethyl)phosphine hydrochloride (TCEP), and dimethyl sulfoxide (DMSO) were obtained from Sigma Aldrich (Steinheim, Germany). Poly-L-lysine(20)-g[3.5]-PEG(2) and PLL(20)-g[3.5]-PEG(3.4)-biotin were obtained from SuSoS (Dübendorf, Switzerland). NeutrAvidin, 200 nm NeutrAvidin-labelled, and amine-modified polystyrene beads were obtained from Thermo Fisher Scientific (Massachusetts, USA). Sodium acetate (>98.5%), acetic acid (100%), and phosphate-buffered saline (PBS, pH = 7.4) were obtained from Carl Roth (Karlsruhe, Germany). HaloTag NHS ligand was obtained from Promega (Wisconsin, USA). The protein constructs denoted as I27 (containing 4 titin I27 domains) and R1-3 (containing talin's rod domains R1 to R3) were expressed and purified as previously described (see next paragraph).[19] PBS buffer was created by diluting 10× PBS concentrate according to the manufacturer's instructions. Sodium acetate buffer (pH = 5) was created by mixing 67 mL of sodium acetate stock (10 mM) with 33 mL acetic acid stock (10 mM). PBS|TCEP buffer was created by adding 1 mM TCEP to the PBS buffer. Sodium acetate|TCEP buffer was created by adding 1 mM TCEP to the sodium acetate buffer. PLL-g-PEG|Biotin solution was created by mixing $2.6 \times 10^{-1}$ g $L^{-1}$ PLL-g-PEG and $3.4 \times 10^{-6}$ g $L^{-1}$ PLL-g-PEG-biotin in PBS|TCEP buffer. NeutraAvidin solution was created by preparing $10^{-3}$ g $L^{-1}$ NeutrAvidin in PBS|TCEP buffer. The construct solution was created by preparing $4.2 \times 10^{-2}$ g $L^{-1}$ I27 or R1-3 and $8.5 \times 10^{-4}$ g $L^{-1}$ biotin-maleimide in sodium acetate|TCEP buffer. The NeutrAvidin-bead solution was prepared by diluting the NeutrAvidin-bead stock solution 1:200 in 1× PBS. The bead solution was prepared by diluting the amine-bead stock solution 1:100 in PBS|TCEP buffer and adding $5 \times 10^{-6}$ g $L^{-1}$ HaloTag NHS ligand.

*Protein Expression and Purification*: Halo-(I27)x2-R1-R2-R3-(I27)x2-His$_6$-Cys construct was expressed using target protein encoding DNA subcloned into a customized pET-based plasmid,[19] which included a C-terminal hexahistidine tag following by a Cys. The plasmids were introduced in *Escherichia coli* BL21-Star cells (ThermoFisher Scientific). Bacterial were pre-cultured in LB-medium containing 100 µg mL$^{-1}$ ampicillin at 37 °C overnight in a shaker. The larger production (1 L) was done in LB-medium containing 100 µg mL$^{-1}$ ampicillin. To induce protein expression at optical density (OD ≈ 600) of 0.4, and 1 mM IPTG was used. Cells were incubated for 12 h at 18 °C after which they were harvested by centrifugation. The Emulsiflex C3 was used for cell lysis and homogenization in 20 mM NaPO$_4$, 500 mM NaCl, and 20 mM imidazole pH 7.4 buffer. The homogenized *E. coli* suspension was centrifuged to get clarified lysate, which then applied to HisTrap FF (5 mL) affinity column (GE healthcare) using chromatography Äkta purifier P100. The Halo-(I27)$_2$-R1-R3-(I27)$_2$-His$_6$-Cys was eluted from column using 20 mM Na$_3$PO$_4$, 500 mM NaCl pH 7.4 buffer with gradually increasing imidazole concentration (20–500 mM). Fractions were directly eluted into microcentrifuge tubes containing 1 mM EDTA, 1 mM DTT.

Eluted fractions were analyzed by SDS-PAGE and Coomassie staining. Furthermore, Halo-(I27)$_2$-R1-R3-(I27)$_2$-His$_6$-Cys construct was purified and buffer exchanged into 1× PBS (containing 1 mM EDTA, 1 mM TCEP) using c. The homogeneity of the purified protein was determined to be up to 90% by SDS-PAGE and it was detected in Western blot analysis using $\alpha$-His HRP with 1:4000 dilution. In addition, the purity of protein also confirmed by dynamic light scattering (DLS), Malvern ZetaSizer ZS, which indicated that protein was pure and homogenous. For long-term storage, sample was aliquoted and flash-frozen for −80 °C storage.

*Microfluidic Channel Preparation and Functionalization*: Microfluidic channels were prepared using PDMS-based soft lithography and plasma-based bonding of the PDMS-channel on silica cover glasses (#1.5 coverslips, 15 mm; Menzel, Germany) as previously reported.[20,33] Directly before bonding, the cover glasses were cleaned using the RCA-1 procedure.

For the stretching experiments involving PLL-g-PEG linkers, the microfluidic channel was equilibrated by washing with 1× PBS buffer at 25 µL min$^{-1}$ for 10 min. Afterward, the PLL-g-PEG|Biotin solution was incubated at 17 µL min$^{-1}$ for 30 min and then washed with 1× PBS buffer at 25 µL min$^{-1}$ for 10 min. Subsequently, NeutrAvidin-beads were incubated at 17 µL min$^{-1}$ for several minutes until sufficient coverage (approximately 1000–2000 beads per FoV) was reached and then washed with 1× PBS buffer at 25 µL min$^{-1}$ for 12 min.

For the stretching experiments involving the I27 and R1-3 protein constructs, the microfluidic channel was equilibrated by washing with PBS|TCEP buffer at 25 µL min$^{-1}$ for 10 min. Afterward, PLL-g-PEG|Biotin solution was incubated at 17 µL min$^{-1}$ for 30 min and then washed with PBS|TCEP buffer at 25 µL min$^{-1}$ for 10 min. Subsequently, NeutrAvidin was incubated at 17 µL min$^{-1}$ for 15 min and again washed as mentioned previously. Then the biotinylated construct (I27 or R1-3) was incubated at 17 µL min$^{-1}$ for 30 min and then washed as mentioned previously. Finally, the beads were applied on the surface at 10 µL min$^{-1}$ for several min until sufficient coverage (approximately 1000 beads per FoV) was reached and then washed with PBS|TCEP buffer at 10 µL min$^{-1}$ for 5 min.

*Microfluidics-Based Force Experiments*: All measurements were performed on a Nikon Eclipse Ti-E microscope (Nikon, Düsseldorf, Germany) equipped with a 100× Plan-Apo oil immersion objective (NA 1.45), a Lumen 200 (Prior Scientific, Cambridge, UK) white light source, and an Andor Zyla 4.2 sCMOS camera (2048 × 2048 pixels; Oxford Instruments, Oxford, UK). The measurements were done using a ND4 neutral density intensity filter, $1 \times 1$ binning of the sCMOS camera and using a dichroic filter set optimized for green fluorescent protein (GFP; excitation: 482 nm ± 9 nm, dichroic filter: 495 nm, emission: 520 nm ± 14 nm). For the stretching experiments involving PLL-g-PEG linkers, an additional 1.5× relay lens was used, resulting in a pixel size of 43.3 nm with a FoV of ≈90 × 90 µm$^2$, and images were recorded with an acquisition rate of 10 Hz (i.e., 100 ms time lag between two frames) and an exposure time of 50 ms. Measurements involving the I27 and R1-3 constructs were done without adding the relay lens (i.e., at a pixel size of 65 nm and a FoV of ≈135 × 135 µm$^2$) and at an acquisition rate of 4 Hz (i.e., 250 ms time lag between two frames; 20 ms exposure time). Flow rates between 5 and 300 µL min$^{-1}$ or 50 and 1500 µL min$^{-1}$ (as indicated in the main manuscript), applied in a block- or stepwise profile, were generated by syringe pumps (WPI, #AL1000-2202) using 1 mL syringe (HSV, #4200.000V0) for functionalization reagent injection and 20 mL syringe (HSV, #4200.000V0) filled with buffer (1× PBS or PBS|TCEP) for washing and flow-based force generation. Bead displacement curves were extracted from these measurements using a previously described, custom-made single-particle tracking library.[33] This library was extended by additional procedures, which corrected the measurement for the drift of the sample (see Section S1, Supporting Information), extracted force and extension information with single-bead resolution (using the model described in Section S2, Supporting Information), and enabled for a semiautomatic analysis of the obtained data sets using a cluster analysis (Section S3, Supporting Information).

*Steered Molecular Dynamics Simulations*: A model of talin R1-3 (residues 487-909) was prepared using previously resolved structures PDB 1SJ8 and 2L7A. Talin R3 domain (residues 796-909) was prepared using PDB 2L7A. The simulations were performed with Gromacs software[34] using supercomputing facilities provided by CSC, Finland. For the R1-3 construct, the CHARMM36m force field[35] and TIP3P water model in 0.15 M KCl solution were used. For R3 domain, Amber14SB force field[36] with SPC/E water model in 0.15 M KCl[37] was used. The systems were energy minimized and then equilibrated using harmonic position restraints on all heavy atoms of the protein. The temperature and pressure of the R1-3 system was maintained at 310 K and 1 bar using Berendsen algorithm,[38] while for the R3 system, temperature and pressure was maintained at 300 K and 1 bar using V-rescale[39] and Parrinello–Rahman algorithm.[40] Integration time step of 2 fs was used in all the simulations.

The R1-3 model was first equilibrated for 100 ns, and then subjected to unfolding in steered molecular dynamics by the end-to-end distance extension using constant velocity pulling at 2 nm ns$^{-1}$. Three independent replicas were performed for the unfolding using steered molecular dynamics.

Talin R3 domain was equilibrated for 10 ns, and then unfolded in steered molecular dynamics simulations using 0.1 nm ns$^{-1}$ pulling velocity. Five independent replicas were generated for the unfolding of R3.

Visualization of the structure snapshots was performed using PyMOL.

## Supporting Information

Supporting Information is available from the Wiley Online Library or from the author.

## Conflict of Interest

The authors declare no conflict of interest.

## Data Availability Statement

The data that support the findings of this study are available from the corresponding author upon reasonable request.

[1] E. Evans, *Annu. Rev. Biophys. Biomol. Struct.* **2001**, *30*, 105.
[2] K. Neuman, A. Nagy, *Nat. Methods* **2008**, *5*, 491.
[3] A. del Rio, R. Perez-Jimenez, R. Liu, P. Roca-Cusachs, J. Fernandez, M. Sheetz, *Science* **2009**, *323*, 638.
[4] Y. F. Dufrêne, E. Evans, A. Engel, J. Helenius, H. E. Gaub, D. J. Müller, *Nat. Methods* **2011**, *8*, 123.
[5] I. De Vlaminck, T. Henighan, M. van Loenhout, I. Pfeiffer, J. Huijts, J. Kerssemakers, A. Katan, A. van Langen-Suurling, E. van der Drift, C. Wyman, C. Dekker, *Nano Lett.* **2011**, *11*, 5489.
[6] J. Eyckmans, T. Boudou, X. Yu, C. Chen, *Dev. Cell* **2011**, *21*, 35.
[7] S. Lee, R. Kamm, M. Mofrad, *J. Biomech.* **2007**, *40*, 2096.
[8] V. Hytönen, V. Vogel, *PLoS Comput. Biol.* **2008**, *4*, e24.
[9] M. Paszek, C. DuFort, O. Rossier, R. Bainer, J. Mouw, K. Godula, J. Hudak, J. Lakins, A. Wijekoon, L. Cassereau, M. Rubashkin, M. Magbanua, K. Thorn, M. Davidson, H. Rugo, J. Park, D. Hammer, G. Giannone, C. Bertozzi, V. Weaver, *Nature* **2014**, *511*, 319.
[10] C. Ciobanasu, B. Faivre, C. Le Clainche, *Nat. Commun.* **2014**, *5*, 3095.
[11] M. Yao, B. Goult, H. Chen, P. Cong, M. Sheetz, J. Yan, *Sci. Rep.* **2014**, *4*, 46.
[12] K. Burridge, P. Mangeat, *Nature* **1984**, *308*, 744.
[13] H. Chen, P. Appeddu, J. Parsons, J. Hildebrand, M. Schaller, J. Guan, *J. Biol. Chem.* **1995**, *270*, 16995.
[14] D. Critchley, A. Gingras, *J. Cell Sci.* **2008**, *121*, 1345.
[15] D. Critchley, *Annu. Rev. Biophys.* **2009**, *38*, 235.
[16] K. Austen, P. Ringer, A. Mehlich, A. Chrostek-Grashoff, C. Kluger, C. Klingner, B. Sabass, R. Zent, M. Rief, C. Grashoff, *Nat. Cell Biol.* **2015**, *17*, 1597.
[17] M. Yao, B. Goult, B. Klapholz, X. Hu, C. Toseland, Y. Guo, P. Cong, M. Sheetz, J. Yan, *Nat. Commun.* **2016**, *7*, 11966.
[18] R. Tapia-Rojo, Á. Alonso-Caballero, J. Fernández, *Proc. Natl. Acad. Sci. USA* **2020**, *117*, 21346.
[19] A. Haining, M. von Essen, S. Attwood, V. Hytönen, A. del Río Hernández, *ACS Nano* **2016**, *10*, 6648.
[20] S. Block, B. Fast, A. Lundgren, V. Zhdanov, F. Höök, *Nat. Commun.* **2016**, *7*, 12956.
[21] R. R. Netz, D. Andelman, *Phys. Rep.* **2003**, *380*, 1.
[22] F. Oesterhelt, M. Rief, H. E. Gaub, *New J. Phys.* **1999**, *1*, 6.
[23] S. Liese, M. Gensler, S. Krysiak, R. Schwarzl, A. Achazi, B. Paulus, T. Hugel, J. Rabe, R. R. Netz, *ACS Nano* **2017**, *11*, 702.
[24] C. Yuan, A. Chen, P. Kolb, V. Moy, *Biochemistry* **2000**, *39*, 10219.
[25] F. Pincet, J. Husson, *Biophys. J.* **2005**, *89*, 4374.
[26] M. R. Uhlig, C. A. Amo, R. Garcia, *Nanoscale* **2018**, *10*, 17112.
[27] G. I. Bell, *Science* **1978**, *200*, 618.
[28] F. Rico, V. T. Moy, *J. Mol. Recognit.* **2007**, *20*, 495.
[29] F. Rico, A. Russek, L. Gonzalez, H. Grubmüller, S. Scheuring, *Proc. Natl. Acad. Sci. USA* **2019**, *116*, 6594.
[30] R. Merkel, P. Nassoy, A. Leung, K. Ritchie, E. Evans, *Nature* **1999**, *397*, 50.
[31] J. M. Teulon, Y. Delcuze, M. Odorico, S. W. W. Chen, P. Parot, J. L. Pellequer, *J. Mol. Recognit.* **2011**, *24*, 490.
[32] S. B. Fowler, R. B. Best, J. L. T. Herrera, T. J. Rutherford, A. Steward, E. Paci, M. Karplus, J. Clarke, *J. Mol. Biol.* **2002**, *322*, 841.
[33] P. Jönsson, A. Gunnarsson, F. Höök, *Anal. Chem.* **2010**, *83*, 604.
[34] M. J. Abraham, T. Murtola, R. Schulz, S. Páll, J. C. Smith, B. Hess, E. Lindahl, *SoftwareX* **2015**, *1–2*, 19.
[35] J. Huang, S. Rauscher, G. Nawrocki, T. Ran, M. Feig, B. L. de Groot, H. Grubmüller, A. D. MacKerell, *Nat. Methods* **2016**, *14*, 71.
[36] J. A. Maier, C. Martinez, K. Kasavajhala, L. Wickstrom, K. E. Hauser, C. Simmerling, *J. Chem. Theory Comput.* **2015**, *11*, 3696.
[37] I. S. Joung, T. E. Cheatham III, *J. Phys. Chem. B* **2008**, *112*, 9020.
[38] H. J. Berendsen, J. P. Postma, W. F. van Gunsteren, A. DiNola, J. R. Haak, *J. Chem. Phys.* **1984**, *81*, 3684.
[39] G. Bussi, D. Donadio, M. Parrinello, *J. Chem. Phys.* **2007**, *126*, 014101.
[40] M. Parrinello, A. Rahman, *J. Appl. Phys.* **1981**, *52*, 7182.